Shape of storms facilitates energy transfer from weather to deep ocean

Noel G. Brizuela, Eric A. D'Asaro, Jennifer MacKinnon

Peer Review status as of June 28, 2026:

This is a non-peer reviewed preprint submitted to EarthXiv. The manuscript has been submitted for review at *Science Advances*.

Shape of storms facilitates energy transfer from weather to deep ocean

Noel G. Brizuela[1*], Eric A. D'Asaro[2] Jennifer MacKinnon[3]

[1]Max Planck Institute for Meteorology, Hamburg, Germany.

[2]Applied Physics Laboratory, University of Washington, Seattle, USA.

[3]Scripps Institution of Oceanography, University of California San Diego, La Jolla, USA.

[*]Corresponding author. Email: noel.brizuela@mpimet.mpg.de

Near inertial internal waves (NIWs) play a key role in transferring energy from extratropical storms into the ocean interior, where they drive turbulence that influences large scale circulation and climate. Efficient downward propagation of NIW energy requires horizontal wavelengths of order 100 km, yet NIWs are conventionally assumed to be generated with much longer scales near 1000 km, requiring subsequent modification by ocean vorticity gradients. Here, we reformulate the equations in terms of vorticity and divergence and show that mesoscale convective systems within storms naturally imprint scales ~100 km onto the NIW field, enabling efficient downward energy propagation. Storm morphology may be an important control on the transfer of energy from the atmosphere to the ocean interior; its multi-decadal changes may lead to similar changes in mixing at depth.

When a storm moves over the ocean its winds generate near-inertial oscillations within the ocean's surface mixed layer (ML). The storm's effects can eventually reach all depths, as near-inertial internal waves (NIWs) propagate down from the ML and transfer energy from the episodic winds of weather to currents in the ocean interior (*1, 2*). NIWs thereby enhance turbulent mixing

of the upper ocean and permanent thermocline, thus helping sustain large scale patterns of ocean heat storage that shape background climate (*3–5*).

How fast the NIWs can propagate downward shortly after storm passage depends on the wavelength (L) of ML currents induced by a storm's winds (*2, 6*). As ML currents rotate clockwise in time under the influence of Earth's rotation, they induce cycles of divergence that pump the ML base up and down and enable downward energy transfer (*7*). Oscillating vertical velocities associated with this *inertial pumping* scale as $1/L$, while the downward group velocity of NIWs follows $1/L^2$ (*8*). As a result, NIW energy from a storm that imprints scales $L \sim 100$ km onto the ML will propagate 100 times faster than the energy from a storm that generates currents with wavelengths $L \sim 1000$ km (*7*).

Extratropical storms (ETs) that move eastward across the midlatitudes are the primary source of NIW energy (*9–11*). Theoretical works of NIW generation typically assume that ETs drive ML motions with scales $L \sim 1000$ km and thus induce negligible inertial pumping. The scaling $L \sim 1000$ km is set by the distance $L \sim 2\pi U_{storm}/f$ traveled in an inertial period $2\pi/f$ by a storm that translates at speed U_{storm} (*12*). Downward propagation of storm-driven energy under these conditions happens only after weeks or months, but countless observations show NIWs propagating down promptly after the passage of ETs. To reconcile theoretical numerics and empirical evidence, oceanographers have sought to quantify NIW refraction by background and planetary vorticity gradients that would shorten L, enhance inertial pumping, and accelerate the downward propagation of NIW energy in the wake of ETs (*6, 13–15*).

Theoretical and modeling studies on the refraction and propagation of NIWs often model ETs as a spatially-constant wind stress such that $L \rightarrow \infty$ and shorter scales must emerge from oceanic rather than atmospheric processes (*16–20*). Ample evidence certainly shows that ocean eddies can steer and energize NIWs (*15, 21–24*). Still, the assumption in theoretical studies that ETs force NIWs with $L \rightarrow \infty$ erases any possibility that the complex morphology of ETs actively shapes NIW propagation. To understand NIW-eddy interactions in realistic settings, we must first clarify the true scales and features that NIWs inherit directly from ETs.

Realistic simulations exist where the ocean is forced by reanalysis or simulated winds that reflect the true shape of ETs and mesoscale features embedded in them (*3, 11, 25, 26*). A recent study applied sophisticated spatial filters to one of such simulations and found NIWs with short

L being forced directly under ETs (*27*). However, it remains unclear whether direct forcing of small-scale NIWs results from atmospheric, oceanic, or coupled mechanisms.

The assumption that ETs lack the length scales necessary to induce inertial pumping contradicts our most basic knowledge about the storms' dynamics and morphology. It ignores the fact that ETs are powered by baroclinic energy conversion within narrow ($L \sim 100$ km) atmospheric fronts where warm and cold air masses meet and convection occurs (*28, 29*). Low-level winds associated with these fronts have a geostrophic vortical component and strong ageostrophic convergence that allows for convective cloud formation and storm intensification (*30*). Therefore, weather fronts and other mesoscale convective systems ensure that wind fields under ETs include features with a wide range of spatial scales.

Fully coupled models with storm-resolving atmospheric components are becoming increasingly popular for use in multidecadal climate projections (*31, 32*). As global warming brings about changes in the characteristics of ETs (*33–35*), spatiotemporal patterns of NIW generation, propagation, and subsequent turbulent mixing are likely to change in both models and reality. Probing and understanding these changes requires new frameworks that acknowledge mesoscale convective features within ETs and help relate their properties to patterns in NIW activity.

Here, we show that the morphology of ETs and associated weather fronts enables the immediate generation of inertial pumping under ETs and thus accelerates downward propagation of NIWs. Successive forcing by convergent and vortical winds that surround convective regions in ETs is very similar to the conditions under tropical cyclones, whose ability to generate inertial pumping and propagating NIWs has long been recognized (*12, 36, 37*). We estimate that the shape of storms is ~100 times more important in generating inertial pumping under ETs than refraction by the planetary vorticity gradient (β). This result implies that subsequent eddy-NIW interactions are actively shaped by mesoscale features in weather and that global patterns of NIW propagation and mixing may respond to long-term changes in storm morphology.

Vorticity-divergence view of NIW generation

It is well established that ETs are powered by atmospheric fronts and convective features with $L \sim 100$ km. But snapshots of the horizontal wind stress $\vec{\tau} = (\tau_x, \tau_y)$ acting on the ocean surface

are dominated by larger features spanning thousands of kilometers (Fig. 1a). To highlight the smaller fronts and lows embedded in weather, we plot both $\vec{\tau}$ and its divergence ($\nabla \cdot \vec{\tau}$) and curl ($\hat{k} \cdot \nabla \times \vec{\tau}$) (Fig. 1b). Visual comparison between these two versions of weather makes clear that i) every storm is associated with small scale gradients, and ii) these smaller features cannot be easily identified using $\vec{\tau}$ alone.

In what follows, we revisit NIW generation under ETs using a linear model forced by both $\nabla \cdot \vec{\tau}$ and $\hat{k} \cdot \nabla \times \vec{\tau}$. This change in variables is convenient because it yields equations that explicitly include inertial pumping (*7, 38*). A full derivation of the equations used is presented in the Supplementary Material.

Let us consider the rigid lid, linear dynamics of a ML driven by $\vec{\tau}$ and damped by a friction parameter r (*39*). In such a scenario, winds give rise to currents $\vec{u} = \vec{u}_E + \vec{u}_I$ that include a slowly-varying Ekman component $\vec{u}_E = (u_E, v_E)$ and inertially-rotating perturbations $\vec{u}_I = (u_I, v_I)$. One may assume that $\partial\vec{u}/\partial t \sim \partial\vec{u}_I/\partial t$ and thus solve separately for $\vec{u}_E$ and $\vec{u}_I$ (see Supplementary Material). Rewriting $\vec{u}_I$ in complex form $\mathbf{Z}_I = u_I + iv_I$, leads to the condition

$$\frac{\partial \mathbf{Z}_I}{\partial t} = -\omega \mathbf{Z}_I - \frac{1}{\omega}\frac{\partial \tilde{\mathbf{F}}}{\partial t}, \tag{1}$$

where $\omega = if + r$ and $f = f_0 + \beta y$ is the Coriolis parameter on a β plane. Momentum forcing is given by $\tilde{\mathbf{F}} = (\tau_x + i\tau_y)/(\rho_0 h_0)$, such that momentum fluxes are spread evenly across a ML of constant density ρ_0 and thickness h_0 (*40, 41*). All simulation output showed here is based on representative values $\rho_0 = 1024$ kg m^{-3} and $h_0 = 50$ m.

At the same time, we solve for the divergence $\mu_I = \nabla \cdot \vec{u}_I$ and vorticity $\xi_I = \hat{k} \cdot \nabla \times \vec{u}_I$ of ML motions. The time evolution of their complex sum $\mathbf{\Sigma}_I = \mu_I + i\xi_I$ is given by the curl and divergence of Eq. (1) or can be derived independently from the full conservation laws for μ_I and ξ_I in a multilayer flow (see Supplementary Material). Either way, after we assume linearity, impose a rigid lid, and subtract Ekman solutions, we get

$$\frac{\partial \mathbf{\Sigma}_I}{\partial t} = -\omega \mathbf{\Sigma}_I - \frac{1}{\omega}\frac{\partial \tilde{\mathbf{G}}}{\partial t} + \beta\left(\frac{1}{\omega^2}\frac{\partial \tilde{\mathbf{F}}}{\partial t} - \mathbf{Z}_I\right). \tag{2}$$

Notice that the first and second terms in Eq. (2) have the same form as the oscillator in Eq. (1). The term $-\omega\mathbf{Z}_I$ induces inertial rotations in the (u_I, v_I) plane, and these translate onto oscillations in (μ_I, ξ_I) space and are captured by the identical term $-\omega\mathbf{\Sigma}_I$ (*38*). Meanwhile, atmospheric

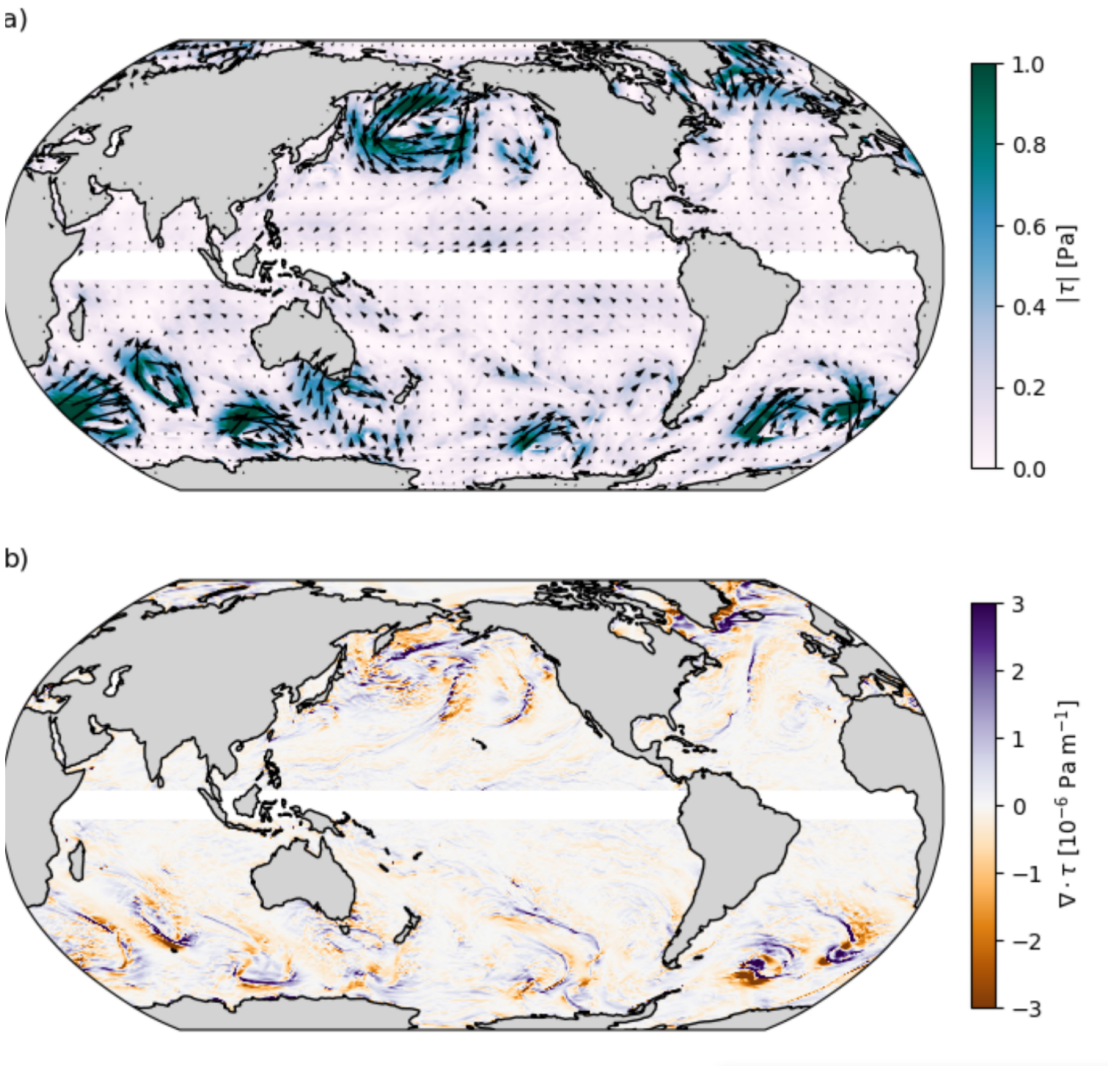

Figure 1: Wind stress vectors and gradients reveal contrasting scales under ETs. Wintertime snapshots of a) the wind stress τ and b) its horizontal divergence $\nabla \cdot \tau$ show ETs moving across all ocean basins.

momentum forcing enters Eq. (2) via $\tilde{\mathbf{G}} = (\nabla \cdot \vec{\tau} + i\hat{k} \cdot \nabla \times \vec{\tau})/(\rho_0 h_0)$, which replaces $\tilde{\mathbf{F}}$ and thus allows wind gradients to imprint themselves onto inertial oscillations.

Accelerations in (u_I, v_I) will initially follow the direction of winds and later deviate under the effects of ω. Similarly, the evolution of (μ_I, ξ_I) will initially mirror the spatial structure of atmospheric forcing but later fall into oscillations where momentum is transferred between vortical and divergent modes of motion (*38*). As μ_I oscillates, the ML thickness will follow $\partial h/\partial t \approx -h_0 \mu_I$, such that oscillations in $\mathbf{\Sigma}_I$ imply the occurrence of inertial pumping. Notice that the oscillator in

Eq. (2) is forced by both $\nabla \cdot \vec{\tau}$ or $\hat{k} \cdot \nabla \times \vec{\tau}$, so inertial pumping can arise from either a vortical or a divergent wind stress pattern.

The third term in Eq. (2) accounts for the effects of vorticity transport by horizontal currents, whose curl and divergence help drive divergence and vorticity, respectively (*42*). Contributions from this linear term capture the planetary vorticity gradient β and can lead to inertial pumping even under spatially-homogeneous atmospheric forcing (*14*). However, we'll show that the evolution of $\mathbf{\Sigma}_I$ is overwhelmingly dictated by the direct forcing term $-\omega^{-2}\,\partial\tilde{\mathbf{G}}/\partial t$ and the shape of storms exerts a greater influence on pumping than β.

Sample solutions of $\mathbf{Z}_I$ and $\mathbf{\Sigma}_I$ were forced using wind stress data from the ERA5 reanalysis (*43*). A detailed view of solutions under a North Pacific ET show the impulsive generation of inertial pumping by a weather front (Fig. 2). The ET's wind field spans many hundreds of kilometers (Fig. 2A), but temporal variations $\partial\tilde{\mathbf{G}}/\partial t$ have much smaller length scales and peak along a frontal region that runs from north to south (Fig. 2B). Gradients under these narrow fronts act as the dominant forcing in Eq. (2) and thus excite inertial pumping immediately upon their passage, as evidenced by deviations $h - h_0$ in the western half of Fig. 2C. The rich spatial structure of $h - h_0$ shows that inertial pumping and scales $L \sim 100$ km can arise directly below an ET without the slow and gradual action of β or nonlinear interactions with background mesoscale currents.

Oscillations in $\mathbf{Z}_I$ and $\mathbf{\Sigma}_I$ are excited at the same time and are both driven by the same atmospheric feature (Figs. 2D-G). The front forces $\mathbf{Z}_I$ via rapid changes in the wind stress magnitude and direction (Fig. 2D), while $\mathbf{\Sigma}_I$ is excited by variations in the curl and divergence of $\vec{\tau}$ (Fig. 2E). Complex spatial patterns in $h - h_0$ point to the diversity of wave phases across the region in Fig. 2C, which allows pressure gradient forces to act on stratified ocean layers below. This ultimately means that ET winds alone can drive wind-driven momentum to propagate into the ocean interior (*7*).

Below, we show that the impulsive generation of inertial pumping by translating weather fronts can happen across the extratropical ocean, and not only under the ET pictured in Fig. 2. To do so, we compare the contributions of terms including β and of the wind stress gradients $\tilde{\mathbf{G}}$ in driving the variance $|\mathbf{\Sigma}_I|^2$.

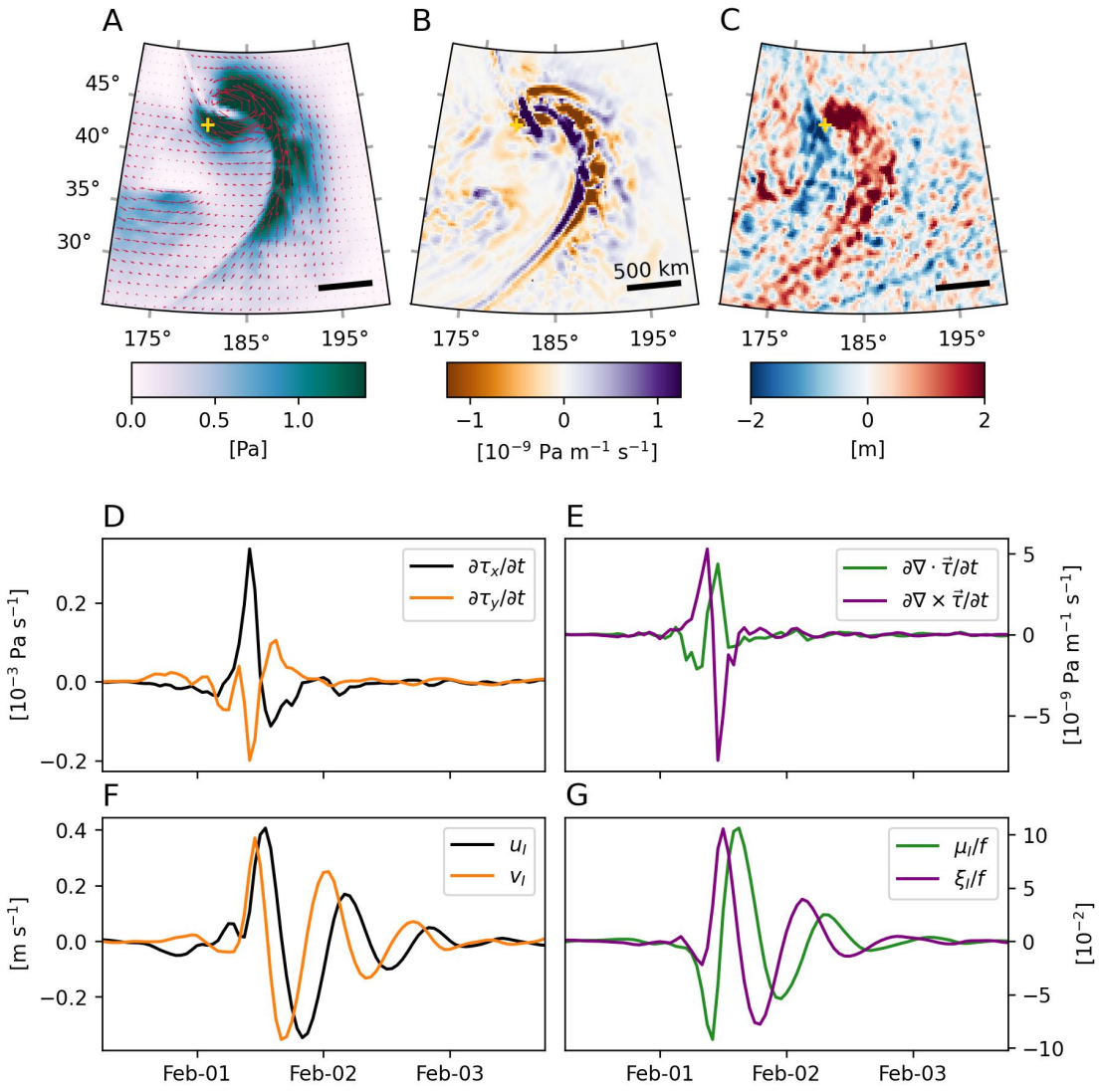

Figure 2: Inertial pumping in the wake of an ET. Snapshots of A) $\vec{\tau}$ (vectors), its magnitude $|\vec{\tau}|$ (color shading), and B) divergence $\partial\nabla\cdot\vec{\tau}/\partial t$ show the structure of an ET and its fronts. The storm's imprint on the ML is evidenced by C) deviations $h - h_0$ obtained via Eq. (2) and linear continuity. Time series at 180°E, 43°N (yelow cross in panels A-C) show the D,E) atmospheric forcing and F,G) simulated ocean response according to Eqs. (1) and (2). Solutions highlight how both F) $\mathbf{Z}_I = u_I + iv_I$ and G) $\mathbf{\Sigma}_I = \nabla\cdot\vec{u}_I + i\nabla\times\vec{u}_I$ are simultaneously forced by the translating front highlighted in B).

Resonant shapes in oceanic and atmospheric weather

Given the expression for kinetic energy $E_k \approx \frac{1}{2}\rho_0 h_0 |\mathbf{Z}_I|^2$ *(40, 41)*, one can use Eq. (1) to write the rate of kinetic energy input from winds onto oscillations in $\mathbf{Z}_I$ as

$$\Pi_{E_k} = \rho_0 h_0 \overset{7}{\mathrm{Re}}\left(\frac{-\mathbf{Z}_I^*}{\omega}\frac{\partial\tilde{\mathbf{F}}}{\partial t}\right). \tag{3}$$

Π_{E_k} peaks when temporal rotation in $\tilde{\mathbf{F}}$ becomes resonant with $\mathbf{Z}_I$ (*40, 44*). ETs that move eastward along the midlatitudes often drive such resonant forcing, as the wind direction rotates clockwise under translating fronts and low pressure systems (*40*). Therefore, Π_{E_k} is greatest along the midlatitude storm tracks (Fig. 3a) (*9, 10, 45, 46*). However, the power transfer captured by Π_{E_k} may or may not translate onto patterns of downward energy propagation by NIWs (*8, 11, 47–50*).

Oscillatory solutions $\mathbf{\Sigma}_I$ may be used to derive an expression for the rate of change in the available potential energy (E_a, see Materials and Methods) of NIWs, which is

$$E_a = g\,\delta\rho(h - h_0)^2/2 \approx \frac{g h_0^2}{8f^2}\delta\rho\,|\mathbf{\Sigma}_I|^2. \tag{4}$$

Here, the relation between E_a and $|\mathbf{\Sigma}_I|^2$ exists because cycles in $\mathbf{\Sigma}_I$ imply oscillations in μ_I that can be integrated in time to obtain $h - h_0$. This integration is achieved by a factor $(h_0/2\omega)^2$, and is therefore only valid for periods when $\mathbf{\Sigma}_I$ oscillates freely. $\delta\rho$ represents a density shift across the ML base, and h_0 is the ML depth. Both of these values are expected to vary significantly across the ocean, but here we use $\delta\rho = 1$ kg m^{-3} and $h_0 = 50$ m for demonstration purposes. Multiplying Eq. (2) by $\mathbf{\Sigma}_I^*$ yields an equation for $\frac{1}{2}\frac{\partial|\mathbf{\Sigma}_I|^2}{\partial t}$ that we substitute into Eq. (4) to obtain the contributions to E_a from wind stress gradients

$$\Pi_{E_a}^G = \delta\rho\frac{g h_0^2}{4f^2}\mathrm{Re}\left(\frac{-\mathbf{\Sigma}_I^*}{\omega}\frac{\partial\tilde{\mathbf{G}}}{\partial t}\right) \tag{5}$$

and from the β effect

$$\Pi_{E_a}^\beta = \delta\rho\frac{g\,\beta\,h_0^2}{4f^2}\mathrm{Re}\left(\frac{\mathbf{\Sigma}_I^*}{\omega^2}\frac{\partial\tilde{\mathbf{F}}}{\partial t} - \mathbf{\Sigma}_I^*\mathbf{Z}_I\right). \tag{6}$$

Note that the ratio of these two quantities does not depend on the values chosen for $\delta\rho$ and h_0. Eq. (5) accounts for resonance between $\tilde{\mathbf{G}}$ and $\mathbf{\Sigma}_I$, such that $|\mathbf{\Sigma}_I|^2$ and E_a grow when $\tilde{\mathbf{G}}$ rotates clockwise in the $(\nabla\cdot\vec{\tau}, \hat{k}\cdot\nabla\times\vec{\tau})$ plane, thus following the same progression that the term $-\omega\mathbf{\Sigma}_I$ imposes on Eq. (2). This way, resonant forcing of inertial pumping requires that a convergent wind stress be followed by one with positive vorticity, then by a divergent one, and so on (*38*).

In contrast, resonance in Eq. (6) relies on alignment between the phases of $\mathbf{\Sigma}_I$ and the advection of background vorticity gradients by $\mathbf{Z}_I$. For example, ML currents $\mathbf{Z}_I = u_I + iv_I$ advect the background vorticity gradient β, and a value $v_I < 0$ induces convergence that raises ζ_I. Similarly, $u_I < 0$ induces a curl in the vorticity transport that acts to increase μ_I (*42*). This way, interactions between $\mathbf{Z}_I$ and β can act to amplify $\mathbf{\Sigma}_I$, but also suppress existing gradients in the ML flow.

Time-averaged values of $\Pi^G_{E_a}$ and $\Pi^\beta_{E_a}$ for the winter of 2022 (DJF, year randomly chosen) exemplify how temporal variations in $\tilde{\mathbf{G}}$ make greater contributions to inertial pumping than β (Figs. 3B,C). Spatial patterns differ between both quantities, but widespread values $\Pi^G_{E_a} > 2\times10^{-6}$ W m^{-2} over much of the northwestern and central Pacific, are at least one order of magnitude greater than values of $\Pi^\beta_{E_a}$. This generalizes the impression from Fig. 2 that inertial pumping will typically arise immediately in the wakes of weather fronts and not only gradually upon wave refraction. Furthermore, negative values of $\Pi^\beta_{E_a}$ over much of the central North Pacific indicate that inertial pumping driven by $\partial\tilde{\mathbf{G}}/\partial t$ was often attenuated, rather than amplified, by β-refraction.

Overall contributions to E_a may be calculated as the time- and space- integrals of $\Pi^G_{E_a}$ and $\Pi^\beta_{E_a}$, which yield roughly 5 and 620×10^{12}J within the area and 3-month period represented in Figs. 3B,C. Therefore, NIWs in our solutions obtained ~120 times more E_a from $\partial\tilde{\mathbf{G}}/\partial t$ than they did from β-refraction. This ratio is roughly 5 times lower when we consider only latitudes between 25°N and 37°N, as this precludes most areas where $\Pi^\beta_{E_a} < 0$ (Fig. 4A). Our result thus indicates that convergent and divergent features in weather are first-order drivers of extratropical patterns of inertial pumping and NIW propagation.

Regional peaks in Π_{E_k} and $\Pi^G_{E_a}$ are both aligned with the midlatitude storm tracks (Figs. 3A,B). This happens because the conditions for resonant forcing of $\mathbf{Z}_I$ under a translating storm are often met at the same time as the conditions for resonant forcing of $\mathbf{\Sigma}_I$ (e.g. Fig. 2). Nonetheless, local maxima in Π_{E_k} are spatially broad while features in $\Pi^G_{E_a}$ follow much finer scales, with some peaks resembling the width and alignment of individual weather fronts as if they were frozen in time. Therefore an ET may efficiently power $\mathbf{Z}_I$ throughout its lifespan, but the degree of resonance between $\mathbf{\Sigma}_I$ and mesoscale convective systems appears to be more dynamic and variable.

As is expected for NIWs, whose near-f frequency tethers their velocity vectors close to the horizontal plane, the total energy $E_k + E_a$ in our simulations is dominated by E_k. Accordingly, the wind work Π_{E_k} is three orders of magnitude greater than $\Pi^G_{E_a}$ (Fig. 3). Still, the fact that NIWs here have any E_a means that they are super-inertial and able to propagate vertically. The broad presence of inertial pumping across the North Pacific (Figs. 2C, 3B) therefore points to the widespread generation of superinertial, multiscale NIWs that can promptly propagate into the ocean interior.

Under the traditional representation of ETs as a spatially-constant wind stress, Fig. 3B would be zero everywhere and Fig. 3C would be positive everywhere, with β acting only to enhance inertial

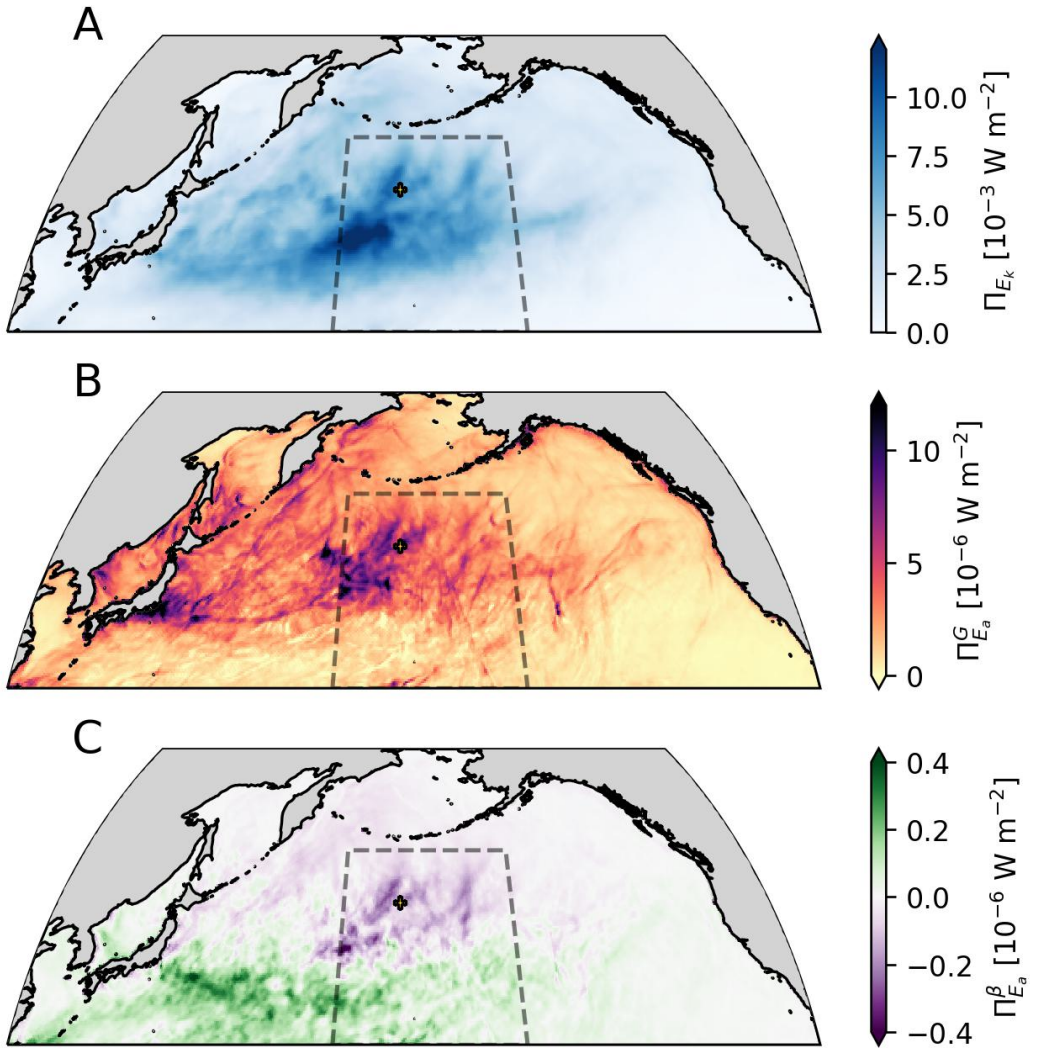

Figure 3: Kinetic and potential energy input from winds into the NIW field. Rates of A) kinetic and B-C) potential energy transfer are estimated using Eqs. (3)-(6). Solutions to the slab models in Eqs. (1) and (2) were forced using reanalysis data of $t\vec{a}u$ between December of 2020 and February of 2021. B) Quantifies the effects of spatial gradients in the surface wind stress, while C) accounts for the β effect. Estimates in B) and C) assume $h_0 = 50$ m ans $\delta\rho = 1$ kg m^{-3}.

pumping (*14, 51*). However, long-term averages of zonally-integrated, wintertime $\Pi^G_{E_a}$ and $\Pi^\beta_{E_a}$ across the North Pacific reaffirm a more nuanced reality (Fig. 4A). Our results confirm that $\partial\tilde{\mathbf{G}}/\partial t$ is the primary driver of $\mathbf{\Sigma}_I$, and further show that β persistently acts to dampen inertial pumping poleward of 40°N (albeit with minimal impacts). This stands against the assumption that β will always enhance pumping and results from systematic phase relations between $\mathbf{Z}_I$, $\partial\tilde{\mathbf{F}}/\partial t$, and the

wind-driven $\mathbf{\Sigma}_I$ (Eq. 6). Understanding the latitudinal sign-change of β will require a more thorough analysis of ET morphology and spatial patterns in near-inertial oscillations that arise from it.

Implications for weather-climate interactions

NIWs impact climate by transferring energy from weather onto currents in the stratified ocean. This ultimately leads to turbulence that enables diffusive heat fluxes between the surface ocean and the stratified interior (*3, 5*). If ML oscillations driven by ETs only had scales $L \sim 1000$ km, patterns of downward NIW propagation and subsequent diffusive heating would likely follow the latitudinal dependence of β and the spatial distribution of mesoscale eddies that shorten L via refraction (*19, 20, 52*). However, persistent generation of inertial pumping by ET winds reveal the morphology of mesoscale convective systems as a first-order factor setting spatial patterns of energy transfer from weather to the ocean interior (Fig. 4A).

Early analyses of wind-driven NIW generation revealed multidecadal trends in $|\mathbf{Z}_I|$ (*46*) but could not infer whether enhanced $\mathbf{Z}_I$ would alter the energetics of the ocean interior. However, solutions to Eqs. (1) and (2) reveal striking similarities in the spatial patterns of $\Pi^G_{E_a}$ and Π_{E_k} (Fig. 4A), suggesting that long-term changes in $\mathbf{Z}_I$ will be mirrored by $\mathbf{\Sigma}_I$.

In fact, we find significant multidecadal trends in North Pacific wintertime values of both $|\mathbf{Z}_I|$ and $|\mathbf{\Sigma}_I|$ (Fig. 4B,C). Trends exhibit nearly identical spatial patterns, which point to a northward migration of NIW activity. This is consistent with the well-documented poleward shift of the storm tracks (*33, 54, 55*), as trends are generally positive north of 40°N and negative to the south of that latitude, and this change in sign is roughly aligned with climatological peaks in $|\mathbf{Z}_I|$ and $|\mathbf{\Sigma}_I|/f$ (black contours in Figs. 4B,C).

As changes in ET activity reshape the oceanic NIW field, thermocline mixing and subsequent downward heat fluxes will also be modified. As such, the role of NIWs in climate may evolve as a function of the intensity, translation, and shape of ETs. Climate simulations with storm-resolving horizontal resolutions (*31, 56*) are becoming increasingly common and may allow us to view NIW energy propagation as a mediator of ocean-atmosphere coupling, rather than as a static consequence of atmospheric chaos.

Known trends in mesoscale eddy activity (*57*) are likely to further influence long-term changes

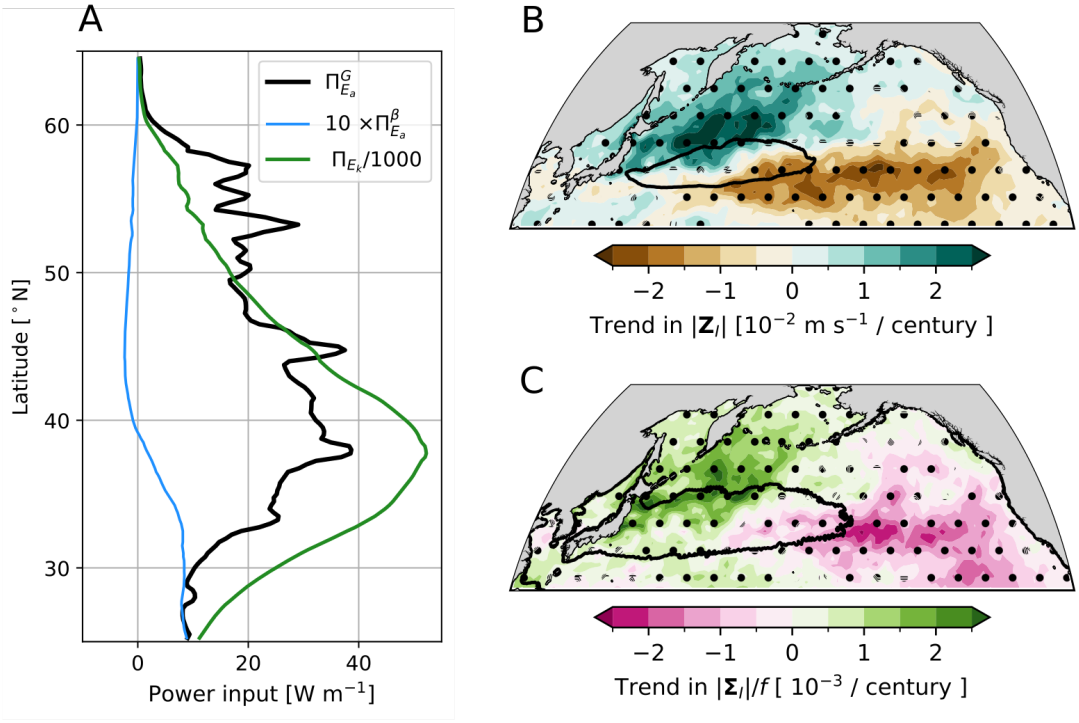

Figure 4: Long-term energetics and trends in wintertime North Pacific NIWs between 1983 and 2022. A) shows zonally-integrated values of (black) $\Pi^G_{E_a}$, (blue) $10 \times \Pi^\beta_{E_a}$, and (green) $\Pi_{E_k}/1000$, with the two latter scaled for comparison purposes. Trends in simulated wintertime B) $|\mathbf{Z}_I|$ and C) $|\mathbf{\Sigma}_I|/f$ reveal multidecadal changes in NIW activity. Trends were computed using a regional Mann-Kendall test (*53*) and black dots indicate regions were trends are statistically significant. Black contours outline areas where climatological wintertime values exceed threshold values B) $|\mathbf{Z}_I|$ >0.045 m/s and C) $|\mathbf{\Sigma}_I|/f > 4.5 \times 10^{-3}$.

in NIW propagation and mixing. Gradients in geostrophic vorticity are known to refract NIWs and modify the conditions for resonant wave generation (*18, 49*). While our analyses have focused on the isolated effects of wind stress gradients, future studies ought to explore the joint effects of realistic storm morphology and a complex oceanic background. Grasping the full scope of these interactions will require accounting for air-sea interactions that systematically distort near-surface winds over mesoscale ocean eddies (*58*).

Conclusion

We have shown that weather fronts embedded in ETs can directly drive inertial pumping and thus efficiently transfer energy to the ocean interior. This contradicts the typical assumption that ETs only generate NIWs with $L \sim 1000$ km and thus depend entirely on refraction to induce substantial inertial pumping. Our insight is enabled by Eq. (2), which reformulates the well-known NIW slab model in terms of spatial gradients rather than horizontal currents (*38*). Furthermore, our results rely on the inclusion of hourly reanalysis data with $1/4°$ horizontal resolution (*43*) that resolves fronts at the leading edge of ETs (Fig. 1).

Previous analyses had argued that translating storms generate NIWs with length scales $L = 2\pi\, U_{storm}/f$ (*12*). This yields $L \approx 800$ km for a typical value for the translation speed $U_{storm} = 12$ m s^{-1} at 40 °N and describes NIWs whose phase is steady in a storm-following frame of reference (*59*). Inertial pumping at such length scales appears immediately in the wake of ETs and serves as the background for a more complex broadband response to impulsive forcing by weather fronts (Fig. 2C).

Research in the last decades has been guided by the assumption that extratropical NIWs rely entirely on refraction and other oceanic processes to acquire short lengthscales and impact the thermocline force balance. Our results deny this assumption and further suggest that the changing dynamics of mesoscale convective systems will help regulate the multidecadal evolution of patterns in NIW propagation and mixing in the ocean interior (Fig. 4). To form a holistic view of NIWs and their role in climate, future research will have to recognize how NIW properties arise from complex interactions between ETs, their morphology, and the underlying oceanic eddy field.

References and Notes

1. G. Veronis, Partition of energy between geostrophic and non-geostrophic oceanic motions. *Deep Sea Research (1953)* **3** (3), 157–177 (1956).

2. J. Kroll, The propagation of wind-generated inertial oscillations from the surface into the deep ocean. *Journal of Marine Research* **33** (1975).

3. M. Jochum, *et al.*, The impact of oceanic near-inertial waves on climate. *Journal of Climate* **26** (9), 2833–2844 (2013).

4. J. A. MacKinnon, *et al.*, Climate process team on internal wave–driven ocean mixing. *Bulletin of the American Meteorological Society* **98** (11), 2429–2454 (2017).

5. N. Gutiérrez Brizuela, *et al.*, Prolonged thermocline warming by near-inertial internal waves in the wakes of tropical cyclones. *Proceedings of the National Academy of Sciences* **120** (26), e2301664120 (2023).

6. E. A. D'Asaro, *et al.*, Upper-ocean inertial currents forced by a strong storm. Part I: Data and comparisons with linear theory. *Journal of Physical Oceanography* **25** (11), 2909–2936 (1995), doi:https://doi.org/10.1175/1520-0485(1995)025⟨2909:UOICFB⟩2.0.CO;2.

7. A. Gill, On the behavior of internal waves in the wakes of storms. *Journal of Physical Oceanography* **14** (7), 1129–1151 (1984).

8. M. H. Alford, J. A. MacKinnon, H. L. Simmons, J. D. Nash, Near-inertial internal gravity waves in the ocean. *Annual Review of Marine Science* **8**, 95–123 (2016).

9. M. Alford, Internal swell generation: The spatial distribution of energy flux from the wind to mixed layer near-inertial motions. *Journal of Physical Oceanography* **31** (8), 2359–2368 (2001), doi:https://doi.org/10.1175/1520-0485(2001)031⟨2359:ISGTSD⟩2.0.CO;2.

10. A. Rimac, J.-S. von Storch, C. Eden, H. Haak, The influence of high-resolution wind stress field on the power input to near-inertial motions in the ocean. *Geophysical Research Letters* **40** (18), 4882–4886 (2013), doi:https://doi.org/10.1002/grl.50929.

11. J.-S. von Storch, V. Lüschow, Wind power input to ocean near-inertial waves diagnosed from a 5-km global coupled atmosphere-ocean general circulation model. *Journal of Geophysical Research: Oceans* **128** (2), e2022JC019111 (2023), doi:doi.org/10.1029/2022JC019111.

12. J. F. Price, Internal wave wake of a moving storm. Part I. Scales, energy budget and observations. *Journal of Physical Oceanography* **13** (6), 949–965 (1983).

13. E. Kunze, Near-inertial wave propagation in geostrophic shear. *Journal of Physical Oceanography* **15** (5), 544–565 (1985), doi:https://doi.org/10.1175/1520-0485(1985)015⟨0544:NIWPIG⟩2.0.CO;2.

14. E. A. D'Asaro, The decay of wind-forced mixed layer inertial oscillations due to the β effect. *Journal of Geophysical Research: Oceans* **94** (C2), 2045–2056 (1989).

15. L. N. Thomas, *et al.*, Direct observations of near-inertial wave ζ-refraction in a dipole vortex. *Geophysical Research Letters* **47** (21), e2020GL090375 (2020).

16. N. Balmforth, S. G. Llewellyn Smith, W. Young, Enhanced dispersion of near-inertial waves in an idealized geostrophic flow. *Journal of marine research* **56** (1), 1–40 (1998).

17. P. Klein, S. L. Smith, G. Lapeyre, Organization of near-inertial energy by an eddy field. *Quarterly Journal of the Royal Meteorological Society: A journal of the atmospheric sciences, applied meteorology and physical oceanography* **130** (598), 1153–1166 (2004).

18. D. B. Whitt, L. N. Thomas, Resonant generation and energetics of wind-forced near-inertial motions in a geostrophic flow. *Journal of Physical Oceanography* **45** (1), 181–208 (2015), doi:https://doi.org/10.1175/JPO-D-14-0168.1.

19. O. Asselin, W. R. Young, Penetration of wind-generated near-inertial waves into a turbulent ocean. *Journal of Physical Oceanography* **50** (6), 1699–1716 (2020), doi:https://doi.org/10.1175/JPO-D-19-0319.1.

20. C. Z. Lazaneo, *et al.*, Interaction of typhoon-driven near-inertial waves with an anticyclone in the Philippine Sea. *Oceanography* **37** (4), 68–81 (2024), doi:doi.org/10.5670/oceanog.2024.308.

21. R. Barkan, *et al.*, Oceanic mesoscale eddy depletion catalyzed by internal waves. *Geophysical Research Letters* **48** (18), e2021GL094376 (2021).

22. X. Yu, *et al.*, Observed equatorward propagation and chimney effect of near-inertial waves in the midlatitude ocean. *Geophysical Research Letters* **49** (13), e2022GL098522 (2022), doi:https://doi.org/10.1029/2022GL098522.

23. G. Liu, *et al.*, Energy transfer between mesoscale eddies and near-inertial waves from surface drifter observations. *Geophysical Research Letters* **50** (16), e2023GL104729 (2023).

24. A. C. Savage, *et al.*, Observations of upper-ocean kinetic energy transfers between near-inertial internal waves and low-frequency dynamics. *Journal of Physical Oceanography* **55** (10), 1625–1643 (2025).

25. H. L. Simmons, M. H. Alford, Simulating the long-range swell of internal waves generated by ocean storms. *Oceanography* **25** (2), 30–41 (2012).

26. A. Delpech, *et al.*, Eddy–internal wave interactions and their contribution to cross-scale energy fluxes: A case study in the California Current. *Journal of Physical Oceanography* **54** (3), 741–754 (2024).

27. J. Rama, C. J. Shakespeare, A. M. Hogg, The wavelength dependence of the propagation of near-inertial internal waves. *Journal of Physical Oceanography* **52** (10), 2493–2514 (2022), doi:doi.org/10.1175/JPO-D-21-0266.1.

28. M. A. Shapiro, D. Keyser, *Fronts, Jet Streams and the Tropopause* (American Meteorological Society, Boston, MA), pp. 167–191 (1990), doi:10.1007/978-1-944970-33-8_10, `https://doi.org/10.1007/978-1-944970-33-8_10`.

29. K. Browning, N. Roberts, Structure of a frontal cyclone. *Quarterly Journal of the Royal Meteorological Society* **120** (520), 1535–1557 (1994), doi:doi.org/10.1002/qj.49712052006.

30. I. Orlanski, B. B. Ross, The evolution of an observed cold front. Part II: Mesoscale dynamics. *Journal of Atmospheric Sciences* **41** (10), 1669–1703 (1984), doi:doi.org/10.1175/1520-0469(1984)041⟨1669:TEOAOC⟩2.0.CO;2.

31. C. Hohenegger, *et al.*, ICON-Sapphire: simulating the components of the Earth system and their interactions at kilometer and subkilometer scales. *Geoscientific Model Development* **16** (2), 779–811 (2023), doi:doi.org/10.5194/gmd-16-779-2023.

32. S. M. Kang, *et al.*, Km-scale coupled simulation and model–observation SST trend discrepancy. *Proceedings of the National Academy of Sciences* **123** (8), e2522161123 (2026), doi:doi.org/10.1073/pnas.2522161123.

33. S.-S. Lee, *et al.*, Interdecadal changes in the storm track activity over the North Pacific and North Atlantic. *Climate Dynamics* **39** (1), 313–327 (2012), doi:doi.org/10.1007/s00382-011-1188-9.

34. J. L. Catto, *et al.*, The future of midlatitude cyclones. *Current Climate Change Reports* **5** (4), 407–420 (2019), doi:doi.org/10.1007/s40641-019-00149-4.

35. V. A. Sinclair, M. Rantanen, P. Haapanala, J. Räisänen, H. Järvinen, The characteristics and structure of extra-tropical cyclones in a warmer climate. *Weather and Climate Dynamics* **1** (1), 1–25 (2020), doi:doi.org/10.5194/wcd-1-1-2020.

36. J. F. Price, Upper ocean response to a hurricane. *Journal of Physical Oceanography* **11** (2), 153–175 (1981), doi:https://doi.org/10.1175/1520-0485(1981)011⟨0153:UORTAH⟩2.0.CO;2.

37. L. K. Shay, R. L. Elsberry, P. G. Black, Vertical structure of the ocean current response to a hurricane. *Journal of Physical Oceanography* **19** (5), 649–669 (1989).

38. N. G. Brizuela, *et al.*, A vorticity-divergence view of internal wave generation by a fast-moving tropical cyclone: Insights from Super Typhoon Mangkhut. *Journal of Geophysical Research: Oceans* p. e2022JC019400 (2023), doi:https://doi.org/10.1029/2022JC019400.

39. R. T. Pollard, R. Millard, Comparison between observed and simulated wind-generated inertial oscillations, in *Deep Sea Research and Oceanographic Abstracts* (Elsevier), vol. 17 (1970), pp. 813–821, doi:https://doi.org/10.1016/0011-7471(70)90043-4.

40. E. A. D'Asaro, The energy flux from the wind to near-inertial motions in the surface mixed layer. *Journal of Physical Oceanography* **15** (8), 1043–1059 (1985), doi:https://doi.org/10.1175/1520-0485(1985)015⟨1043:TEFFTW⟩2.0.CO;2.

41. A. Plueddemann, J. Farrar, Observations and models of the energy flux from the wind to mixed-layer inertial currents. *Deep Sea Research Part II: Topical Studies in Oceanography* **53** (1-2), 5–30 (2006).

42. P. Névir, M. Sommer, Energy–vorticity theory of ideal fluid mechanics. *Journal of the Atmospheric Sciences* **66** (7), 2073–2084 (2009).

43. H. Hersbach, *et al.*, The ERA5 global reanalysis. *Quarterly Journal of the Royal Meteorological Society* **146** (730), 1999–2049 (2020).

44. G. Crawford, W. Large, A numerical investigation of resonant inertial response of the ocean to wind forcing. *Journal of physical oceanography* **26** (6), 873–891 (1996).

45. M. Watanabe, T. Hibiya, Global estimates of the wind-induced energy flux to inertial motions in the surface mixed layer. *Geophysical Research Letters* **29** (8), 64–1 (2002).

46. M. H. Alford, Improved global maps and 54-year history of wind-work on ocean inertial motions. *Geophysical Research Letters* **30** (8) (2003).

47. E. A. D'Asaro, Upper-ocean inertial currents forced by a strong storm. Part II: Modeling. *Journal of Physical Oceanography* **25** (11), 2937–2952 (1995), doi:https://doi.org/10.1175/1520-0485(1995)025⟨2937:UOICFB⟩2.0.CO;2.

48. M. H. Alford, Global calculations of local and remote near-inertial-wave dissipation. *Journal of Physical Oceanography* **50** (11), 3157–3164 (2020), doi:https://doi.org/10.1175/JPO-D-20-0106.1.

49. L. N. Thomas, *et al.*, Why near-inertial waves are less affected by vorticity in the Northeast Pacific than in the North Atlantic. *Oceanography* **37** (4), 10–21 (2024).

50. D. Chaudhuri, *et al.*, Near-inertial response of a salinity-stratified ocean. *Journal of Physical Oceanography* **54** (9), 1841–1855 (2024), doi:doi.org/10.1175/JPO-D-23-0173.1.

51. D. L. Anderson, A. E. Gill, Beta dispersion of inertial waves. *Journal of Geophysical Research: Oceans* **84** (C4), 1836–1842 (1979).

52. D.-K. Lee, P. P. Niiler, The inertial chimney: The near-inertial energy drainage from the ocean surface to the deep layer. *Journal of Geophysical Research: Oceans* **103** (C4), 7579–7591 (1998), doi:doi.org/10.1029/97JC03200.

53. M. Hussain, I. Mahmud, pyMannKendall: a python package for non parametric Mann Kendall family of trend tests. *Journal of open source software* **4** (39), 1556 (2019).

54. Y. Wu, M. Ting, R. Seager, H.-P. Huang, M. A. Cane, Changes in storm tracks and energy transports in a warmer climate simulated by the GFDL CM2. 1 model. *Climate Dynamics* **37** (1), 53–72 (2011), doi:doi.org/10.1007/s00382-010-0776-4.

55. T. Tamarin-Brodsky, Y. Kaspi, Enhanced poleward propagation of storms under climate change. *Nature Geoscience* **10** (12), 908–913 (2017), doi:doi.org/10.1038/s41561-017-0001-8.

56. R. C. Wills, A. R. Herrington, I. R. Simpson, D. S. Battisti, Resolving weather fronts increases the large-scale circulation response to Gulf Stream SST anomalies in variable-resolution CESM2 simulations. *Journal of Advances in Modeling Earth Systems* **16** (7), e2023MS004123 (2024).

57. J. Martínez-Moreno, *et al.*, Global changes in oceanic mesoscale currents over the satellite altimetry record. *Nature Climate Change* **11** (5), 397–403 (2021).

58. C. Conejero, L. Renault, F. Desbiolles, J. McWilliams, H. Giordani, Near-surface atmospheric response to meso-and submesoscale current and thermal feedbacks. *Journal of Physical Oceanography* **54** (3), 823–848 (2024).

59. J. Nilsson, Energy flux from traveling hurricanes to the oceanic internal wave field. *Journal of Physical Oceanography* **25** (4), 558–573 (1995), doi:https://doi.org/10.1175/1520-0485(1995)025⟨0558:EFFTHT⟩2.0.CO;2.

Acknowledgments

Without implying their endorsement, the authors thank Olivier Asselin and Kelsey Malloy for fruitful discussions.

Funding: ————————

Author contributions: Conceptualization: NGB. Methodology: NGB, EAD, and J.M. Formal analysis: NGB. Writing (original draft): NGB. Writing (editing): EAD and JM.

Competing interests: There are no competing interests to declare.

Data and materials availability: ERA5 reanalysis data was obtained from the Copernicus Climate Data Store: https://cds.climate.copernicus.eu/datasets/reanalysis-era5-single-levels?tab=download. Software and sample data used to generate figures in the main text may be downloaded from: .

Supplementary materials

Materials and Methods

References *(7-59)*

Supplementary Materials for

Shape of storms facilitates energy transfer from weather to deep ocean

Noel G. Brizuela*, Eric A. D'Asaro, Jennifer Mackinnon

*Corresponding author. Email: noel.brizuela@mpimet.mpg.de

This PDF file includes:

Materials and Methods

Full derivation of inertial oscillators

The nonlinear dynamics of a multi-layer Boussinesq fluid can be expressed in terms of the two-dimensional velocity vector $\mathbf{u_j} = (u_j, v_j)$ and layer thicknesses h_j as

$$\frac{\partial \mathbf{u}_j}{\partial t} + \mathbf{u}_j \cdot \nabla \mathbf{u}_j + f\hat{k} \times \mathbf{u}_j = -\frac{1}{\rho_j}\nabla p_j + \mathbf{F}_j, \tag{S1}$$

and

$$\frac{\partial h_j}{\partial t} + \mathbf{u}_j \cdot \nabla h_j + h_j \nabla \cdot \mathbf{u}_j = 0, \tag{S2}$$

where the subscript $j = 1, 2, \ldots, n$ labels overlying layers of fluid with densities ρ_j. Layers are counted from the bottom up, such that the surface mixed layer (ML) is noted by $j = n$. $\mathbf{F}_j := (F_j^x, F_j^y)$ defines the vector of external forces acting on each layer and f is the Coriolis frequency. $p_j = g\sum_{l=j+1}^{n} h_l \rho_l$ is the hydrostatic pressure at the top of each layer and $\tilde{h}_j := \sum_{l=1}^{k} h_l$ the height of layer tops above the seafloor.

The same dynamics can be restated in terms of the vorticity ($\xi_j := \hat{k} \cdot \nabla \times \mathbf{u}_j$) and divergence ($\mu_j := \nabla \cdot \mathbf{u}_j$) of each layer (*42*). Under this view, the equations of motion become

$$\frac{\partial \xi_j}{\partial t} = -\nabla \cdot \left[\left(\xi_j + f\right) \mathbf{u}_j \right] + \hat{k} \cdot \nabla \times \mathbf{F}_j, \tag{S3}$$

and

$$\frac{\partial \mu_j}{\partial t} = \hat{k} \cdot \nabla \times \left[\left(\xi_j + f\right) \mathbf{u}_j \right] - \nabla^2 \Psi_j + \nabla \cdot \mathbf{F}_j. \tag{S4}$$

Under this view, the inertial effects of Coriolis and momentum advection are replaced by the divergence and curl of total vorticity transport. Similarly, pressure forces acting on each layer are represented by the scalar Bernoulli function

$$\Psi_j = \frac{1}{2}\mathbf{u}_j^2 + g\left(\tilde{h}_j + \sum_{l=j+1}^{n} h_l \frac{\rho_l}{\rho_j}\right). \tag{S5}$$

Let us first expand Eqs. (S3)-(S4) and convert vectors into complex variables. To do this, we introduce the variables

$$\mathbf{Z}_j := u_j + iv_j \tag{S6}$$

and

$$\tilde{\mathbf{F}}_j := F_j^x + iF_j^y \tag{S7}$$

to represent the flow and the forcing of each fluid layer. Given the differential operator $\mathcal{D} = \left(\frac{\partial}{\partial x} + i\frac{\partial}{\partial y}\right)$, we may also express the dynamics and forcing in terms of complex variables

$$\mathbf{\Sigma}_j := \mu_j + i\xi_j = \mathcal{D}^*\mathbf{Z}_j \tag{S8}$$

and

$$\tilde{\mathbf{G}}_j := \nabla \cdot \mathbf{F}_j + i\hat{k} \cdot \nabla \times \mathbf{F}_j = \mathcal{D}^*\tilde{\mathbf{F}}_j. \tag{S9}$$

Ultimately, the equations of motion are rewritten as

$$\frac{\partial \mathbf{Z}_j}{\partial t} = -\frac{1}{2}\left[\mathbf{Z}_j\mathcal{D}(\mathbf{Z}_j) + \mathbf{Z}_j^*\mathcal{D}(\mathbf{Z}_j^*)\right] - if\mathbf{Z}_j - \frac{1}{\rho_j}\mathcal{D}(p_j) + \tilde{\mathbf{F}}_j \tag{S10}$$

and

$$\frac{\partial \mathbf{\Sigma}_j}{\partial t} = -\{\beta + i\mathcal{D}^*\left[\,\mathrm{Im}(\mathbf{\Sigma}_j)\,\right]\}\mathbf{Z}_j - i\left[f + \mathrm{Im}(\mathbf{\Sigma}_j)\right]\mathbf{\Sigma}_j - \mathcal{D}\left[\mathcal{D}^*(\Psi_j)\right] + \tilde{\mathbf{G}}_j. \tag{S11}$$

Ordered as they appear on the right hand side of Eq. (S10), individual terms represent (i) nonlinear advection, (ii) inertial rotation, (iii) pressure forces, and (iv) external body forcing. Terms in Eq. (S11) may be interpreted in the same way, with the caveat that non-linear advection is now modifying terms for (ii) inertial rotation in the $\mathbf{\Sigma}_j$ plane and (iii) the Bernoulli function.

To describe the linear dynamics of a ML with a rigid lid, we set $j = n$, $\nabla p_n = 0$, and $\Psi_n = 0$. This leaves us with the (much) simpler expressions

$$\frac{\partial \mathbf{Z}_n}{\partial t} = -(if + r)\mathbf{Z}_n + \tilde{\mathbf{F}}_n \tag{S12}$$

and

$$\frac{\partial \mathbf{\Sigma}_n}{\partial t} = -\beta\mathbf{Z}_n - (if + r)\mathbf{\Sigma}_n + \tilde{\mathbf{G}}_n, \tag{S13}$$

where we've introduced the Rayleigh damping parameter r into both equations. Eq. (S12) is the well-known slab model of (*39*) and it yields exactly Eq. (S13) when we compute its curl and divergence (or multiply it by $\mathcal{D}^*$, given $\beta = \partial f/\partial y$). Meanwhile, Eq. (S13) is the slab model used in (*38*) with the sole addition that the β-effect is present and regulates $\mathbf{\Sigma}_n$. Even though Eqs. (S12) and (S13) are mathematically equivalent and express the same physics (Fig. S1), they help account

for different physical properties of the ML response to wind forcing. Eq. (S12) can capture a storm's intensity, while Eq. (S13) is driven by the storm's shape. Despite having the exact same physics embedded in them, both equations account for different information because the forcing $\tilde{\mathbf{G}}_n$ cannot be recovered from knowledge of $\tilde{\mathbf{F}}_n$ at single point in space and viceversa.

We now proceed to isolate the near-inertial component of solutions to the double-decker slab model, and drop the subscript n as we refer only to solutions of the ML flow. Following D'Asaro (1985) (*40*), we separate timescales and obtain the balanced and time-varying linear solutions such that $\mathbf{Z} = \mathbf{Z}_I + \mathbf{Z}_E$ and $\mathbf{\Sigma} = \mathbf{\Sigma}_I + \mathbf{\Sigma}_E$ where slowly-varying solutions are the Ekman balance

$$\mathbf{Z}_E = \frac{1}{\omega}\tilde{\mathbf{F}} \tag{S14}$$

$$\mathbf{\Sigma}_E = \frac{1}{\omega}\tilde{\mathbf{G}} - \frac{\beta}{\omega^2}\tilde{\mathbf{F}}, \tag{S15}$$

where $\omega = if + r$. Decomposing Eqs. (S12) and (S13) into prognostic equations for inertial and steady state components, we can substitute expressions for the temporal derivatives of Ekman solutions and obtain differential equations for the inertial components. This is

$$\frac{\partial \mathbf{Z}_I}{\partial t} = \frac{\partial \mathbf{Z}}{\partial t} - \frac{\partial \mathbf{Z}_E}{\partial t} = -\omega\left(\mathbf{Z}_E + \mathbf{Z}_I\right) + \tilde{\mathbf{F}} - \frac{1}{\omega}\frac{\partial \tilde{\mathbf{F}}}{\partial t} \tag{S16}$$

and

$$\begin{aligned}\frac{\partial \mathbf{\Sigma}_I}{\partial t} =& \frac{\partial \mathbf{\Sigma}}{\partial t} - \frac{\partial \mathbf{\Sigma}_E}{\partial t} \\ =& -\omega\left(\mathbf{\Sigma}_E + \mathbf{\Sigma}_I\right) + \tilde{\mathbf{G}} - \beta\left(\mathbf{Z}_E + \mathbf{Z}_I\right) - \frac{1}{\omega}\frac{\partial \tilde{\mathbf{G}}}{\partial t} + \frac{\beta}{\omega^2}\frac{\partial \tilde{\mathbf{F}}}{\partial t}.\end{aligned} \tag{S17}$$

In both cases, we can use the Ekman balances from Eqs. (S14) and (S15) to cancel terms from Eqs. (S16) and (S17). This leaves us with the linear, near-inertial oscillators

$$\frac{\partial \mathbf{Z}_I}{\partial t} = -\omega\mathbf{Z}_I - \frac{1}{\omega}\frac{\partial \tilde{\mathbf{F}}}{\partial t} \tag{S18}$$

and

$$\frac{\partial \mathbf{\Sigma}_I}{\partial t} = -\omega\mathbf{\Sigma}_I - \frac{1}{\omega}\frac{\partial \tilde{\mathbf{G}}}{\partial t} + \beta\left(\frac{1}{\omega^2}\frac{\partial \tilde{\mathbf{F}}}{\partial t} - \mathbf{Z}_I\right). \tag{S19}$$

Eq. (S19) is identical to the oscillators in (*40*), and Eq. (S18) is its equivalent analogue, where $\mathbf{\Sigma}_I$ has substituted $\mathbf{Z}_I$ and additional terms were added to account for the β-effect on inertial pumping.

Conditions for resonant forcing

As laid out by D'Asaro (1985), one can write a conservation equation for $\frac{1}{2}|\mathbf{Z}_I|^2$ that includes the rate of kinetic energy transfer from winds into NIWs. This is

$$\frac{1}{2}\frac{\partial|\mathbf{Z}_I|^2}{\partial t} = \mathrm{Re}\left(\mathbf{Z}_I^*\frac{\partial\mathbf{Z}_I}{\partial t}\right) = -r|\mathbf{Z}_I|^2 - \mathrm{Re}\left(\frac{\mathbf{Z}_I^*}{\omega}\frac{\partial\tilde{\mathbf{F}}}{\partial t}\right), \tag{S20}$$

whose second term is the wind work that's been used extensively in the literature (*9, 40*).

We follow a similar procedure to derive an expression for the transfer of potential energy E_a from winds into the NIW field. Given the expression

$$E_a = \frac{1}{2}g\delta\rho(h-h_0)^2, \tag{S21}$$

where $\delta\rho = \rho_{n-1} - \rho_n$. Taking the linear continuity relation

$$\frac{\partial h}{\partial t} = -\mathrm{Re}(\mathbf{\Sigma}^I)h_0 \tag{S22}$$

and assuming a wave solution with frequency ω, we can write

$$h = h_0\left[1 + \mathrm{Im}(\mathbf{\Sigma}_I)/\omega\right]. \tag{S23}$$

As a result, the mean deviation $h - h_0$ over an inertial period will be given by $h_0|\mathbf{\Sigma}_I/(2\omega)|$. Further assuming $\omega \approx f$, E_a will be approximately

$$E_a \approx \frac{gh_0^2}{8f^2}\delta\rho\,|\mathbf{\Sigma}_I|^2. \tag{S24}$$

The relation between E_a and $|\mathbf{\Sigma}_I|^2$ is only approximate because it assumes free oscillations and can therefore underestimate the true value of $|h - h_0|$ during the forced stage of a storm. Still, having related these two quantities we can now write an equation for the evolution of $|\mathbf{\Sigma}_I|^2$. This is

$$\begin{aligned}\frac{1}{2}\frac{\partial|\mathbf{\Sigma}_I|^2}{\partial t} &= \mathrm{Re}\left(\mathbf{\Sigma}_I^*\frac{\partial\mathbf{\Sigma}_I}{\partial t}\right)\\ &= -r|\mathbf{\Sigma}_I|^2 + \mathrm{Re}\left(\frac{-\mathbf{\Sigma}_I^*}{\omega}\frac{\partial\tilde{\mathbf{G}}}{\partial t}\right) + \beta\,\mathrm{Re}\left(\frac{\mathbf{\Sigma}_I^*}{\omega^2}\frac{\partial\tilde{\mathbf{F}}}{\partial t} - \mathbf{\Sigma}_I^*\mathbf{Z}_I\right)\end{aligned} \tag{S25}$$

This way, one can take the time derivative of Eq. (S24) and substitute terms in the full expression for $\partial|\mathbf{\Sigma}_I|^2/\partial t$. This explains how to obtain the contributions $\Pi_{E_a}^G$ and $\Pi_{E_a}^\beta$ in the main text.

Implementation with ERA5 data

Hourly data of wind stress from the ERA5 reanalysis (*43*) were used as forcing to drive solutions of Eqs. (1) and (2). The data variables chosen have units of Pa and are listed in the Copernicus Climate Data Store (cds.climate.copernicus.eu/datasets/reanalysis-era5-single-levels) under the names 'aiews' and 'ainss' for the zonal and meridional directions. The vector field ($\vec{\tau}$) made up by these two variables is hourly and has $1/4°$ of horizontal resolution. Horizontal gradients were then computed by central differences to obtain $\nabla \cdot \vec{\tau}$ and $\hat{k} \cdot \nabla \times \vec{\tau}$, which make up $\tilde{\mathbf{G}}$ in Eq. (2).

Data from the North Pacific Ocean between December of 2021 and February of 2022 were used to generate Figs. 2 and 3 in the main text. The snapshot in Figs. 2A-C is from February 1 at 15:00 GMT time, while timeseries in Figs. 2D-G were taken from 180°E, 43°N.

Solutions to Eqs. (1) and (2) were computed in a pointwise fashion, such that solutions at any given point are computed independently of conditions elsewhere. Therefore, gradients $\mu_I = \nabla \cdot \vec{u}_I$ and $\xi_I = \hat{k} \cdot \nabla \times \vec{u}_I$ are not computed by taking numerical gradients of a solution to $\vec{u}_I$. Rather, the gradients are used as the prognostic variables and are directly forced by $\tilde{\mathbf{G}}$ and by terms including β.

To verify that Eqs. (1) and (2) are equivalent statements of ML dynamics, Fig. SS1 compares snapshots of divergence (top row) and vorticity (bottom row) as obtained from both equations. The operator $\mathcal{D}$ is applied to solutions $\mathbf{Z}_I$ to compute gradients, such that Figs. S1A,C show $Re(\mathcal{D}^*\mathbf{Z}_I) = \partial u_I/\partial x + \partial v_I/\partial y$ and $Im(\mathcal{D}^*\mathbf{Z}_I) = \partial v_I/\partial x - \partial u_I/\partial y$. Solutions in the left and right columns of Fig. S1 are identical to visual inspection regardless of the time chosen for comparison. This confirms that Eqs. (1) and (2) and their solutions are indeed physically equivalent.

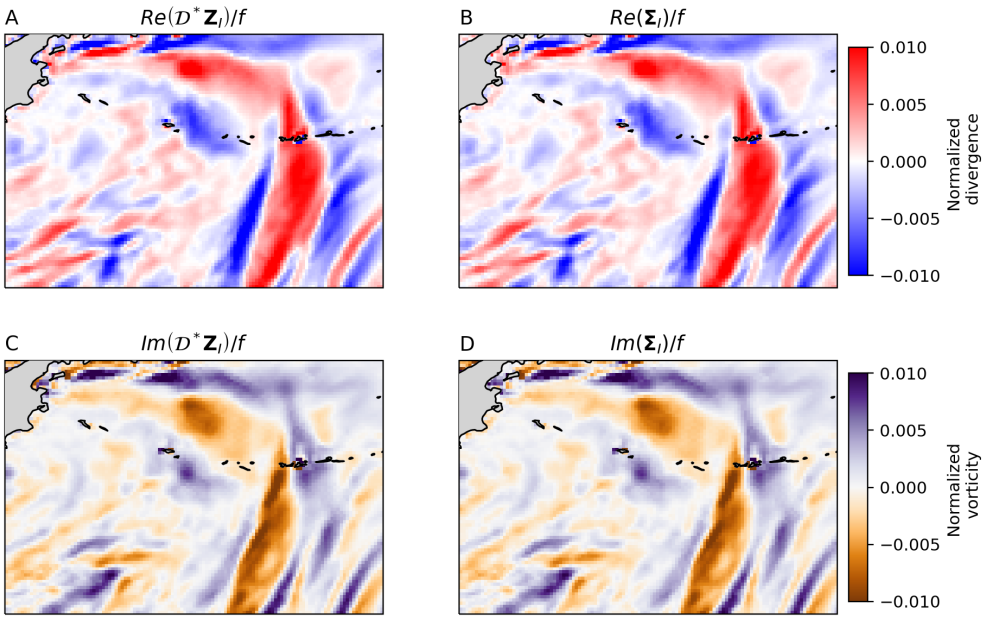

Figure S1: Eqs. (1) and (2) yield equivalent descriptions of mixed layer motions. Snapshots from the North Pacific show values of divergence (top row) and vorticity (bottom row) as computed indirectly from solutions $\mathbf{Z}_I$ of Eq. (1), and as output directly in solutions $\mathbf{\Sigma}_I$ of Eq. (2). A) and C) are computed as the central-difference divergence and curl of $\mathbf{Z}_I$, respectively.